

Needle Insertion Modeling and Simulation

Simon P. DiMaio, *Student Member, IEEE*, and S. E. Salcudean, *Senior Member, IEEE*

Abstract—A methodology for estimating the force distribution that occurs along a needle shaft during insertion is described. An experimental system for measuring planar tissue phantom deformation during needle insertions has been developed and is presented. A two-dimensional linear elastostatic material model, discretised using the finite element method, is used to derive contact force information that is not directly measurable. This approach provides a method for quantifying the needle forces and soft tissue deformations that occur during general needle trajectories in multiple dimensions. The needle force distribution is used for graphical and haptic real-time simulations of needle insertion. Since the force displacement relationship is required only along the needle, a condensation technique is shown to achieve very fast interactive simulations. Stiffness matrix changes corresponding to changes in boundary conditions and material coordinate frames are performed using low-rank matrix updates.

Index Terms—Haptics, needle insertion model, percutaneous intervention, planning, simulation, tissue model, training.

I. INTRODUCTION

ONE OF THE most common procedures employed in modern clinical practice is the subcutaneous insertion of needles and catheters. Such procedures range in complexity from superficial needle sticks to the biopsy of deep-seated tumors, and involve the subcutaneous insertion of long, slender surgical tools and needles into soft, inhomogeneous tissue, usually without visual feedback from below the skin's surface. Physicians and surgeons often rely only upon kinesthetic feedback from the tool, correlated with their own mental three-dimensional (3-D) visualization of anatomic structures.

Complications arising from the complexity of such interventions have been studied in biopsy [1], brachytherapy [2], and particularly, in anaesthesia [3]–[6], where it is found that such complications are due, in large part, to poor technique and needle placement [3].

Virtual reality-based training systems for catheter insertion [7], [8], epidural lumbar puncture [9]–[11], spine biopsy [12], breast biopsy [1], neurosurgical probe insertion [13], interstitial brachytherapy [14], prostate needle biopsy [15], etc., constitute part of the present trend toward computer-based simulators for medical and surgical training [16]. Even experienced physicians are taking advantage of these developments by using simulators to plan and rehearse complex procedures, to design and evaluate new methods or equipment [17], and to control

Manuscript received June 17, 2002; revised June 2, 2003. This paper was recommended for publication by Editor R. Taylor upon evaluation of the reviewers' comments. This paper was presented in part at ICRA 2002, in part at the IEEE-VR Haptics Symposium 2002, and in part at MICCAI 2002.

S. P. DiMaio and S. E. Salcudean are with the Department of Electrical and Computer Engineering, University of British Columbia, Vancouver, BC V6T 1Z4, Canada (e-mail: simond@ece.ubc.ca, tims@ece.ubc.ca).

Digital Object Identifier 10.1109/TRA.2003.817044

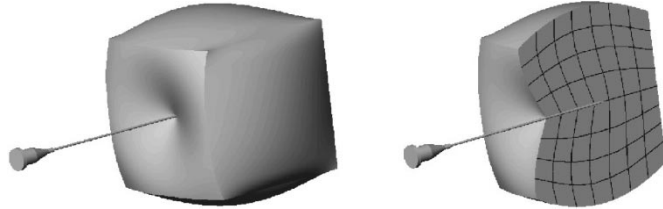


Fig. 1. Needle insertion into soft media.

complex medical robotic systems [18], [19]. The majority of the abovementioned simulation and manipulation systems have been built using largely phenomenological and heuristic models that have not been validated, and that are not generalizable. In some cases, lookup tables determine needle force feedback versus depth for 1-degree-of-freedom (DOF) interaction [7], [20]. Others employ elastic, viscous, and viscoelastic models to approximate needle driving impedance along the axial direction [9], [11]. While perhaps effective for the simulation of predominantly 1-DOF problems, these approaches may not be suitable for problems involving more complex soft tissue anatomy, needle placement optimization, trajectory planning, and automatic control. Indeed, in these cases, more detailed verifiable knowledge of the biomechanical interaction between surgical needles and soft tissues is required.

In prior work, needle insertion forces have been determined for gelatine [21], *ex vivo* porcine, human, and bovine samples [9], [22]. In each case, only the resultant force acting at the proximal end of the needle was measured, while, in fact, penetration forces are distributed along the entire length of the needle axis, resulting from physical phenomena such as cutting, elastic deformation, and friction (static, kinetic, and viscous) [9]. The needle driving forces measured previously are the integration of this force distribution along the needle shaft. Consider the insertion of a needle into a volume of soft material, as depicted in Fig. 1. In general, as the needle penetrates the tissue, forces are applied both axially and laterally and the tissue deforms, affecting the path of the needle and, in turn, the force distribution itself. The resultant proximal force does not provide sufficient information for the tissue deformation to be determined. As it will be shown in this paper, the distribution of forces along the needle plays an important part and should be determined in order to gain insight into the more general biomechanics of needle insertion procedures. Recent work on model-based sensitivity analysis for prostate brachytherapy [23] has already made use of this concept.

This paper presents a new methodology that has been developed to determine needle forces during soft tissue puncture, and is organized as follows. In Section II, an experimental system for measuring planar tissue deformations during probing and needle insertion is described. Material modeling and parameterization

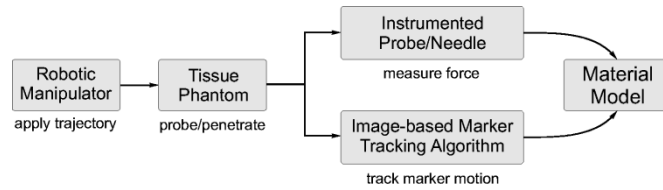


Fig. 2. Needle insertion and probing, experimental procedure.

using a linear elastostatic model, outlined in Section III, are used for estimating the force distribution that occurs along a needle shaft during insertion into a tissue phantom, as is presented in Section IV. The numerical simulation of needle insertion, based upon estimated needle force distributions, is discussed in Section V, particularly because of its relevance for training, planning, and guidance in needle-based procedures. This is extended to real-time simulation for haptics in Section VI, while conclusions and a discussion of future work are provided in Section VII.

II. EXPERIMENTAL SYSTEM TO MEASURE PLANAR TISSUE DEFORMATIONS

Needle insertion and probing experiments proceed as shown in Fig. 2. A 3-DOF, planar robotic manipulator [24] is used to drive an end-effector (blunt probe or needle) into a thin rectangular block of soft elastic material that acts as a tissue phantom. Both tool force and tissue phantom deformation are sampled during the manipulator trajectory, to be used in model identification and verification.

The equipment is shown in Fig. 3, as it is configured during experiments. The soft tissue phantom is molded from polyvinyl chloride (PVC) and a liquid plasticizer, a phthalate ester (Super Soft Liquid Plastic, M-F Manufacturing, TX). By varying the amount of plasticizer added to the PVC, one can produce soft elastic phantoms with elasticities (Young's Modulus) ranging from below 10 kPa (approximately that of breast tissue [1]) to well over 100 kPa, a range that covers many of the body's soft elastic tissues [25]. We use soft tissue phantoms rather than biological tissues because they offer a controlled environment for repeatable experiments; whereas, the inhomogenous nature of biological tissues makes such experiments and validation intractable. It is also unclear whether *ex vivo* tissue samples can provide more relevant results, due to mechanical changes that occur postmortem and during sample preparation. In addition, determining tissue parameters, either *ex vivo* or *in vivo*, is non-trivial [26]–[28]. The needle base driving forces that we measure in the phantoms are of the same order of magnitude as some of the *ex vivo* forces presented in the literature and that we have observed in porcine liver samples. Friction *in vivo* is likely to be lower due to lubrication and higher order effects may be more significant. Results from phantom experiments will help to refine the methodology for future *in vivo* measurements.

The tissue phantom lies upon a horizontal platform and is fixed along the rear face, as shown in Figs. 3, 6, and 7. It is mounted directly below a color complimentary metal–oxide–semiconductor (CMOS) camera and is marked with a grid of black dots, each approximately 2 mm in diameter, that can be tracked by the camera as they move. A silicone

lubricant allows the phantom to slide on the platform, parallel to the camera image plane and needle insertion axis, with very little friction.

A. Motion and Force Sensing

A blunt probing tool and a needle are instrumented with a six-axis force/torque sensor (ATI Nano-17 SI-12-0.12) with 12.5 mN and 0.0625 Nmm force/torque resolution, and can be attached to the 3-DOF planar manipulator, as shown in Fig. 4. The manipulator mechanism moves the end-effector along probing or insertion trajectories.

Force displacement characteristics of a small sample of the tissue phantom were measured by means of an unconfined compression test, as shown in Fig. 5. The measured stress-strain relationship is close to linear up to strains of 15%–20%, but is nonlinear for strains greater than 20%, due to a combination of material and geometric nonlinearities (strain within the sample volume is not uniform). The initial slope (Young's Modulus) is approximately 27 kPa. Subsequent probing and insertion experiments operate with strains below 15%, which is close to the linear force displacement region observed in Fig. 5.

B. Image-Based Deformation Estimation

Images from a single CMOS camera are processed to estimate the two-dimensional (2-D) deformation of the top surface of the tissue phantom. The camera is mounted as shown in Fig. 3, and is interfaced to a PC by a Camera Link Interface. With the given geometry and a camera resolution of 2056×1544 pixels, each pixel width corresponds to a distance of approximately 0.079 mm at the top surface of the tissue phantom. Frames are sampled at 30 Hz and are processed offline by a marker tracking algorithm that tracks 441 individual markers painted onto the top surface of the sample. A correlation-based template matching algorithm locates and tracks the material markers over the entire sequence of image frames. Examples of marker tracking fields are given in Fig. 6. Markers are tracked with subpixel precision.

The camera lens introduces optical aberrations [see Fig. 6(a)] that are compensated by inverting the standard radial-decentering distortion model, which has the following form [29]:

$$\begin{bmatrix} x_p \\ y_p \end{bmatrix} = (1 + k_1 r^2 + k_2 r^4 + k_3 r^6 + \dots) \begin{bmatrix} x_n \\ y_n \end{bmatrix} + \begin{bmatrix} 2p_1 x_n y_n + p_2(r^2 + 2x_n^2) \\ p_1(r^2 + 2y_n^2) + 2p_2 x_n y_n \end{bmatrix} \quad (1)$$

where (x_d, y_d) and (x_n, y_n) are the coordinates of a point projected onto the image plane with and without lens distortion, respectively; r is the distance between (x_n, y_n) and the principle point. Model parameters $P = \{k_1, k_2, k_3, p_1, p_2\}$ are determined in a calibration step. After rectification, optical aberrations account for systematic tracking errors of less than one pixel (<0.1% of tissue phantom width), which has very little impact on estimated marker displacements from frame to frame.

The camera system and marker tracking algorithm measure the motion at the upper surface of the phantom; however, the sample has finite thickness so that needle insertions and boundary probes occur some distance below this surface, as

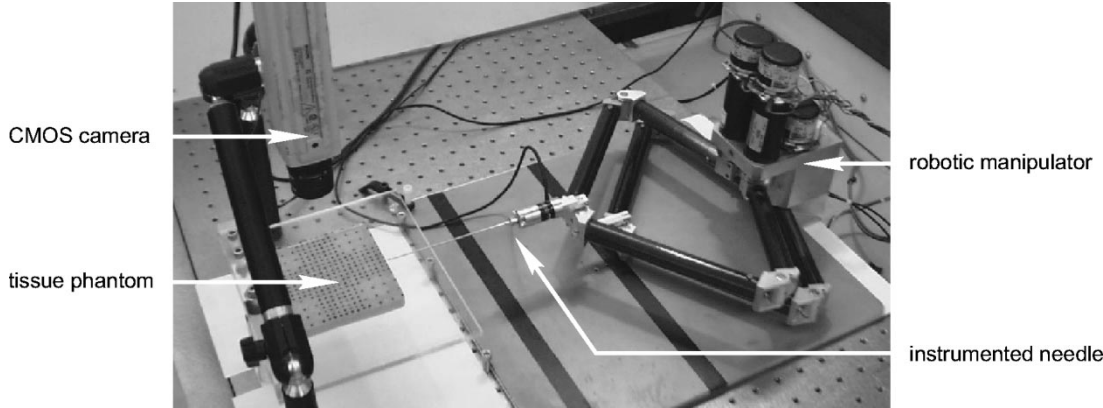


Fig. 3. Complete experimental setup: a robotic manipulator with instrumented epidural needle attached at the end-effector, a tissue phantom and a CMOS camera.

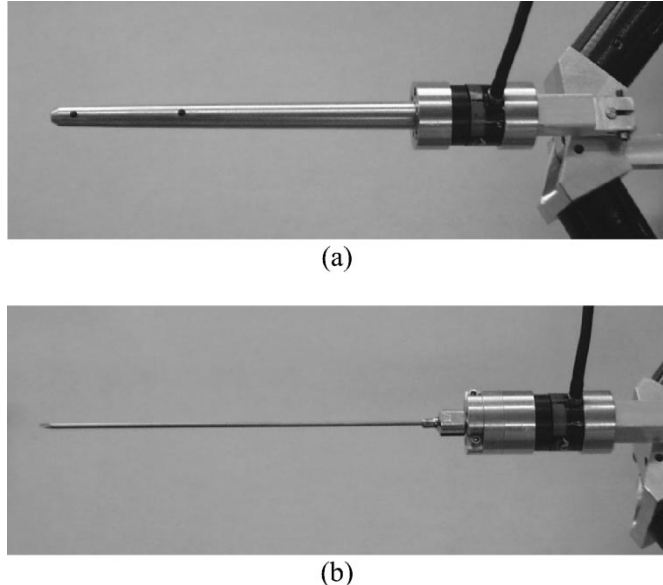


Fig. 4. (a) Instrumented probe. (b) Instrumented 17 gauge Tuohy epidural needle.

illustrated in Fig. 7. Markers could be placed in the needle plane by injecting fiducials [30]; however, this complicates imaging and may affect local material properties. Instead, we use a thin slab of phantom material to minimize error due to deformations perpendicular to the image plane. A thickness of one tenth of phantom width produces small measurement errors while preventing buckling.

III. MATERIAL MODELING AND PARAMETER IDENTIFICATION

For needle force modeling and simulation, it is necessary to characterize the relationship between the forces applied to the tissue phantom, and the resulting phantom deformation. Tissue deformation is complex and is still the subject of much research (e.g., [31]–[33] and many others). In general, tissue modeling is complex because of inhomogeneous, nonlinear, anisotropic elastic and viscous behavior. As a first approximation, this study focuses on homogeneous, linear elastostatic models that predict tissue deformations in two dimensions. Such models are characterized by two parameters, namely Young's Modulus and the Poisson Ratio [34].

A. Linear Elastostatic Model Derivation in Two Dimensions

The elastic material is discretised as shown in Fig. 8. For an elastic continuum, the total strain energy E_{strain} over a solid body Ω , as a function of stress σ and strain ϵ , is given by

$$E_{\text{strain}} = \frac{1}{2} \int_{\Omega} \epsilon^T(x) \sigma(x) dx \quad (2)$$

and is minimized at static equilibrium. With the assumption of a linear relationship between stress σ and strain ϵ , and after discretising (2) using linear shape functions (see [35]), the static equilibrium condition is expressed as

$$\delta E^e = \int_{\Omega^e} A^e \underline{u}^e dx - \underline{f}^e = 0 \quad (3)$$

where each element e reaches its equilibrium state when the first variation of the energy functional δE^e vanishes. The A^e matrix characterizes the elastic behavior of element Ω^e , \underline{u}^e contains the displacement vectors and \underline{f}^e contains the force vectors for those mesh nodes that constitute element e (the applied forces \underline{f}^e are concentrated at mesh nodes) [35]. Over the entire set of elements on body Ω , this leads to a set of $2n$ linear equations

$$K_{(2n \times 2n)} \underline{u} = \underline{f}. \quad (4)$$

B. Model Parameter Identification

In biomechanics studies, tissue model parameters such as Young's Modulus (E) and the Poisson Ratio (ν) are typically determined by testing small homogeneous tissue samples using rheometers and similar materials testing equipment [25]. Measurements of elasticity and viscoelasticity are usually obtained by loading the tissue sample between two parallel plates, in a fashion similar to that shown in Fig. 5. In this work, model parameter identification is achieved by applying known forces to the tissue phantom's boundary, while measuring the resulting node/marker displacements. This approach allows for the measurement of inhomogenous tissue samples, as well as the response due to needle penetration. The set of model parameters $\{E, \nu\}$ that minimizes the squared error between measured and predicted node positions is determined by the following minimization:

$$\min_{E, \nu} (\underline{u} - K(E, \nu)^{-1} \underline{f})^T \cdot (\underline{u} - K(E, \nu)^{-1} \underline{f}) \quad (5)$$

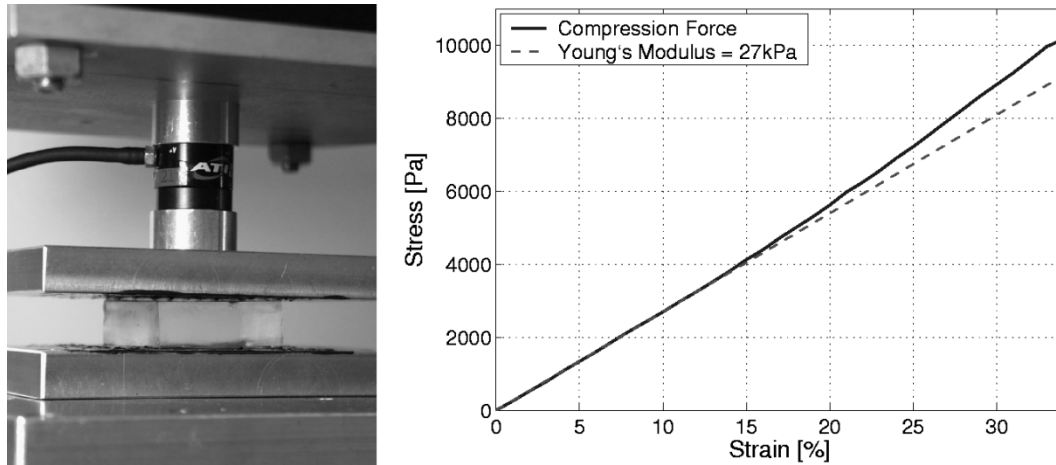


Fig. 5. Compressive loading of a 30 mm × 30 mm × 10 mm material sample. The measured stress-strain relationship is shown on the right (Cauchy stress is used with the assumption of incompressibility).

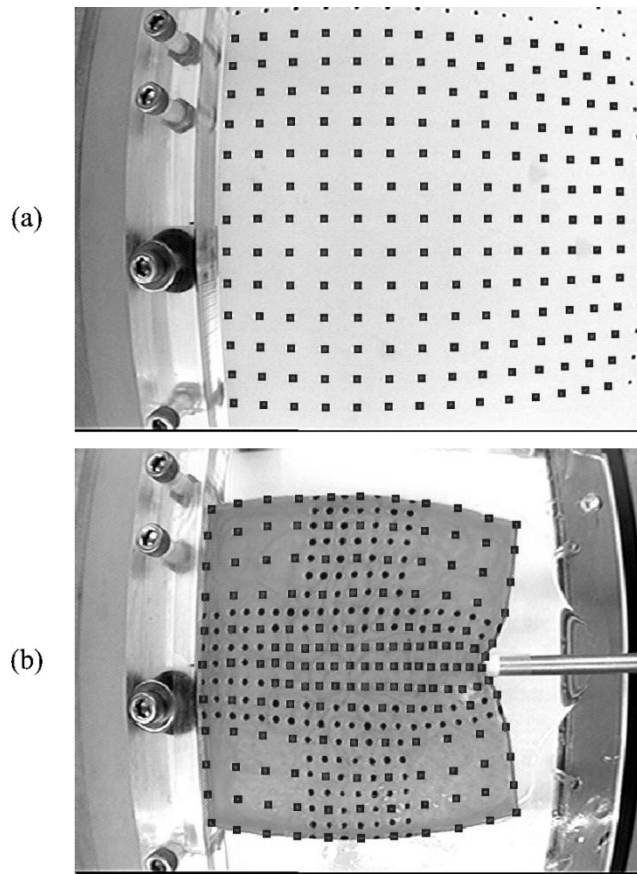


Fig. 6. Image-based marker tracking during (a) calibration and (b) boundary probing. Square search neighborhoods are shown at each tracked marker.

where \underline{u} is the vector of measured model node displacements, \underline{f} is the vector of forces applied to each node by the probe (in this case, the probe is in contact with just one node on the phantom boundary), and K is the system stiffness matrix, which is a function of model parameters E and ν . This problem was solved using a nonlinear least-squares algorithm from the Matlab Optimization Toolbox, which produced consistent results over a large range of initial values.

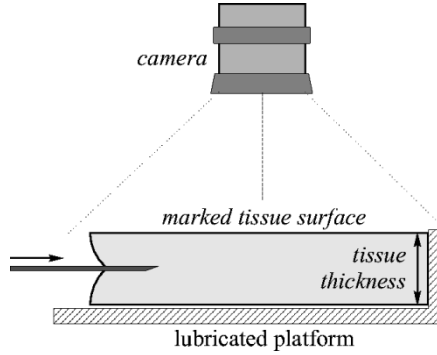


Fig. 7. Profile view of the tissue phantom, illustrating deformation perpendicular to the imaging plane.

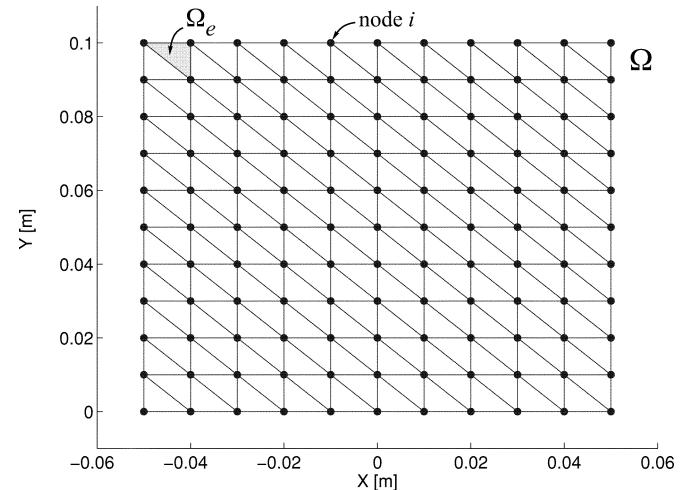


Fig. 8. Continuous domain Ω is divided into a finite number of discrete elements Ω_e by a mesh of nodes.

Tissue phantom motion at several node positions is sampled during boundary probing and is used in conjunction with measured probe force to estimate model parameters E and ν . For small node displacements, the material strains are small, corresponding to the near-linear region of the plot shown in Fig. 5. For the homogeneous tissue phantoms used in experiments, the

squared error is minimized at $E = 25.3$ kPa and $\nu = 0.48$. The Young's Modulus estimate is approximately 6% lower than that measured by the compression test in Section III-A, due to changes in the material stiffness that took place during the period of several days between the boundary probing experiment and the compression test. The plasticizer tends to leak out of the PVC phantoms, so that they become stiffer with time. This has been confirmed in follow-up tests.

Force estimation during needle insertion proceeds using model parameters derived in this manner, which may also be applicable to inhomogeneous, multiphase tissue samples and tissue phantoms.

IV. NEEDLE INSERTION FORCE MODEL

Direct measurement of the needle shaft force distribution by an instrumentation technique is a challenging problem. In the sketch shown in Fig. 1, it is clear that for soft tissues, needle forces result in material motion and deformation; therefore, an indirect means of estimating the applied force distribution is to measure the resulting deformations. If the relationship between applied local forces or stresses and tissue displacement is known, then the distribution of force applied along the needle shaft can be computed.

A. Force Estimates Using a 2-D Model

Clinical needle insertion rates vary between 0.4 and 10 mm per second [21]. In the experiments reported here, a 17-gauge Tuohy epidural needle was inserted into the tissue phantom at several linear velocities from 1 mm/s to 9 mm/s while needle position, insertion force, and tissue phantom deformation were sampled. It is assumed that each sample is a snapshot of static phantom deformation, for which the local strains are low enough (< 15%) that we may consider linear elastic behavior, with a Young's modulus of 25.3 kPa and Poisson ratio of 0.48. Needle flexion and base moments are small and are neglected. These assumptions allow the relationship between 2-D material marker displacements and nodal forces applied by the needle to be characterized using the linear elastostatic model described previously. Given a set of node displacements, the linear elastic model computes the force applied at each node ($\underline{f} = K\underline{u}$ (4), see Section III-A). Model node forces are quite sensitive to small errors in node position measurements; however, because of the random nature of the image-based marker position estimation errors, and the controlled nature of the experiments, it is possible to average several sets of node forces obtained from identical needle insertions, thus improving the estimation result. The needle was inserted into the same phantom, but at different locations for each iteration. We observed force artifacts when needles intercepted or followed previous needle paths; therefore, this had to be avoided. Fig. 9 shows the y axis components of the node forces (the y axis is the direction of insertion), for a needle displacement of approximately 70 mm (from boundary intercept) and insertion velocity of 1 mm/s. Significant external forces are found to occur at nodes lying along the needle shaft. Reaction forces are also visible at the back edge of the model ($y = 0.075$ m) where the phantom is fixed to the platform. Model-based forces estimated at nodes

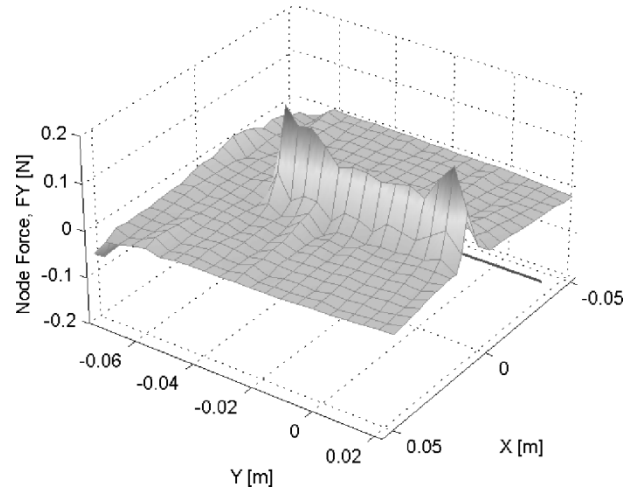


Fig. 9. Tissue phantom forces estimated at model nodes.

lying along the needle shaft are plotted in Fig. 10(a). The force distributions estimated at several instants during a 1 mm/s insertion were integrated by summing node forces that lie along the needle shaft, and were compared with the driving forces measured by the force/torque sensor at the base of the needle. This result is shown in Fig. 11, where there is clearly a large discrepancy between measured and estimated driving force magnitudes. In order to investigate this, the ANSYS finite element analysis software was used to simulate a 3-D model of the tissue phantom.

B. Force Estimates From 3-D Analysis

By comparing 2-D and 3-D simulations, it was determined that the plane strain analysis (4) applied to planar displacement measurements taken at the top surface of the phantom tends to underestimate actual needle shaft forces by approximately 26%, and introduces spurious forces due to out-of-plane deformations that are not accounted for (see Fig. 7). Node force estimates are corrected by the following least-squares minimization:

$$\min_{\underline{F}_s} (\underline{u} - G^{-1}(E, \nu, F_s))^T \cdot (\underline{u} - G^{-1}(E, \nu, F_s)) \quad (6)$$

where the difference between measured and estimated node displacements at the top surface of the phantom is minimized with respect to F_s , the set of node forces that occur along the needle shaft. $G(E, \nu, F_s)$ is a model of the tissue phantom, similar to (4) but in three dimensions, as shown in Fig. 12. ANSYS was used to simulate the model G , and to solve for load forces F_s using a first-order gradient descent algorithm. Node force estimates from the planar model [see Fig. 10(a)] were used to initialize F_s , and some manual intervention was required in order to avoid local minima. The resulting shaft force distributions are illustrated in Fig. 10(b). Note that spurious node forces, such as the peak that appears at the most proximal node on the needle shaft (the insertion point in Fig. 9, disappear after 3-D analysis. The corrected needle force distributions are integrated and once again compared with the measured driving forces, as shown in Fig. 13, where very good agreement between experiment and model results is observed.

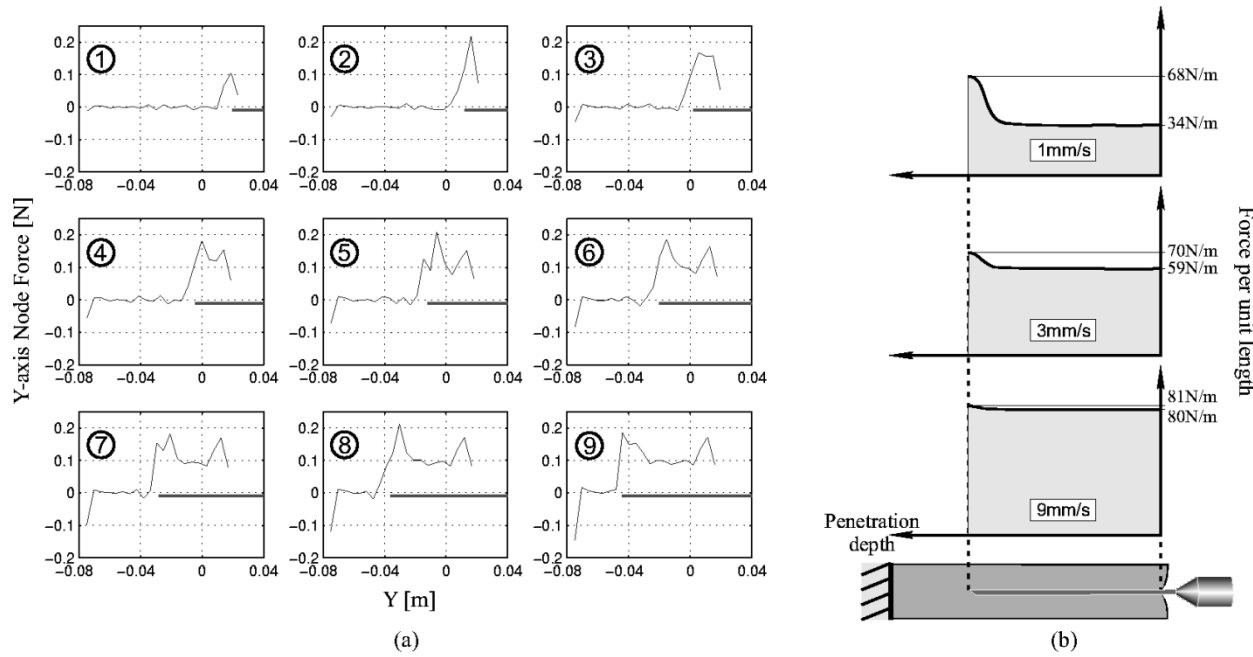


Fig. 10. (a) Tissue phantom forces estimated at nodes along the needle axis at several instants during a 1 mm/s insertion (2-D model). Needle location is shown under each graph. (b) Estimated force distributions along the needle shaft during insertions at several velocities (3-D analysis).

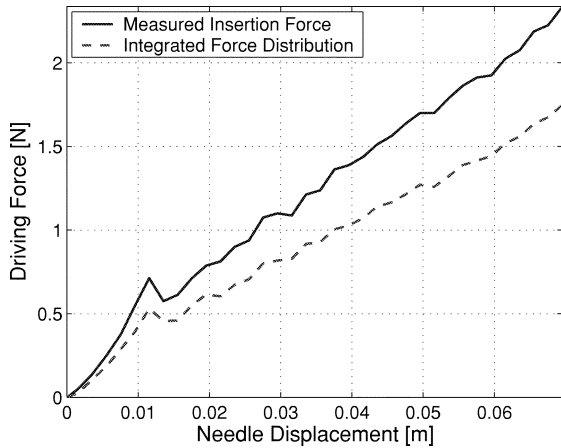


Fig. 11. Comparison of the measured base needle driving force and the integrated needle force distribution (2-D model).

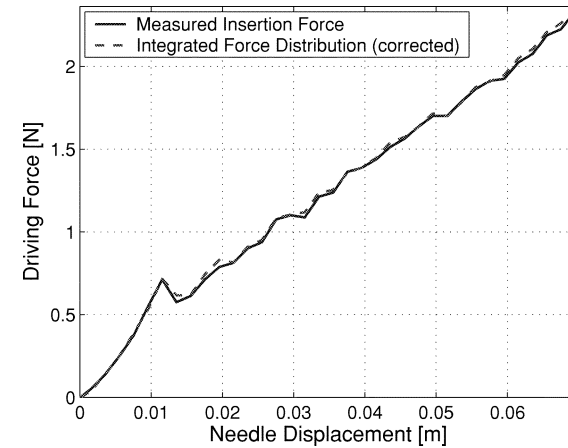


Fig. 13. Comparison of the measured base needle driving force and the integrated needle force distribution (3-D analysis).

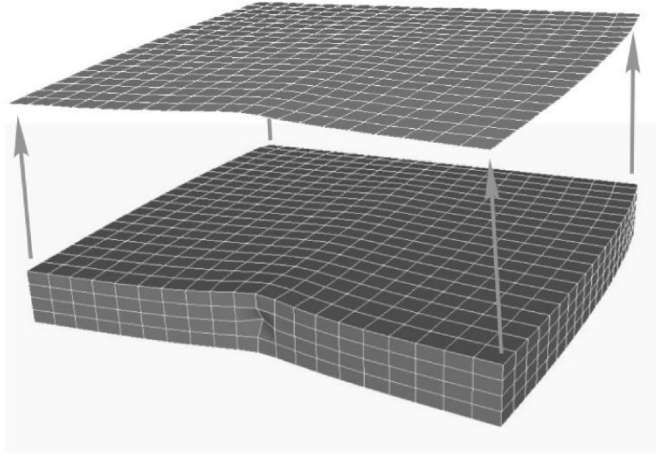


Fig. 12. A 3-D phantom model is used to account for out-of-plane deformations.

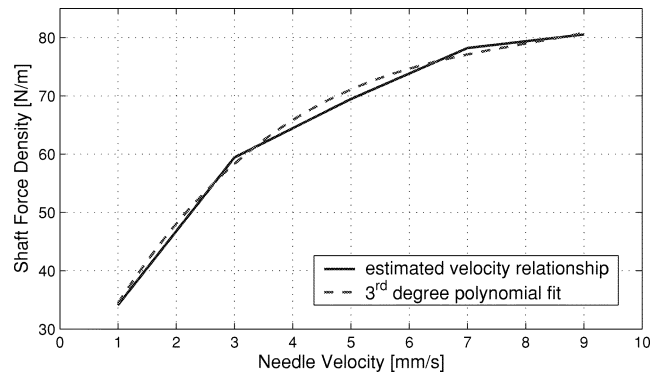


Fig. 14. Relationship between shaft force and needle velocity.

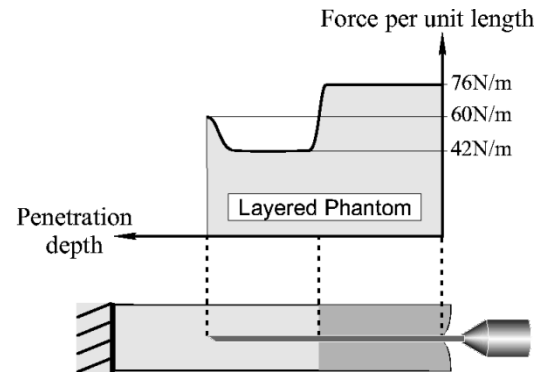
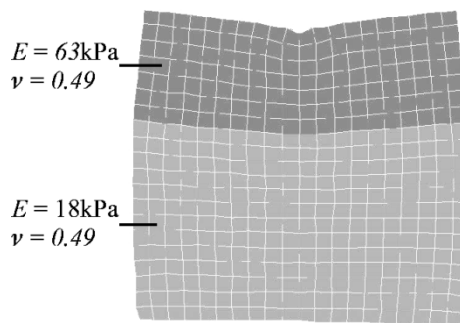


Fig. 15. Shaft force distribution during insertion into a layered inhomogeneous phantom.

Needle insertions were repeated at several driving velocities, and shaft force distributions computed for each case [force distributions for three velocities are shown in Fig. 10(b)]. The relationship between insertion velocity and shaft force “density” (behind the force peak at the needle tip) is graphed in Fig. 14.

The force estimation method generalizes to inhomogeneous materials, and the shaft force distribution estimated during an insertion into a inhomogeneous layered phantom is shown in Fig. 15.

C. Discussion

The 2-D measurements and models have been very helpful in this first attempt to model needle insertion into soft tissues. Errors due to the planar material model, planar deformation measurements, and associated assumptions were limited by using a thin tissue phantom and by correcting force estimates using a 3-D model of the phantom; however, it would be better to use 3-D measurements in future experiments. Accurate 3-D deformation measurements of tissue, or even tissue phantoms, is challenging (see [30]); however, several medical imaging modalities may be used, e.g., computer tomography (CT), magnetic resonance imaging (MRI), Tagged-MRI, and Ultrasound. Given a suitable measurement method, our models and modeling methodology can be applied in 3-D without much difficulty.

The needle force distribution that is estimated from experimental measurements, and used for simulation, indicates that axial forces between the needle and the tissue phantom are relatively uniform along the needle shaft. A force peak, located immediately behind the needle tip, rises approximately 100% above the shaft force, and may be attributable to tissue cutting. In other work, researchers have attempted to separate individual physical contact phenomena such as cutting/fracture and friction, usually by inferring models from forces observed at the base of the needle only. In contrast, we aim to identify contact boundary conditions as a shaft force distribution and to understand how this distribution changes during insertion. This force distribution may incorporate a number of physical contact phenomena such as cutting, elastic deformation, and friction (static, kinetic, and viscous) [9]; however, it is not clear how to decouple these effects, or whether such separation is necessary. The force distribution itself may be useful in developing such models. Instrumentation-based approaches may also be useful for separating force phenomena (e.g., [36]).

Homogeneous tissue phantoms and simple layered phantoms have been used for insertion experiments. This is not representative of typical soft tissues. Future experiments will continue to characterize insertion into tissue phantoms containing several distinct layers and inclusions. Eventually, we hope to be able to use *ex vivo* tissue samples, and finally *in vivo* measurements, where medical imaging modalities such as ultrasound could be used to track speckle, texture, anatomical features, or fiducials.

V. NEEDLE INSERTION SIMULATION

The estimated needle shaft force distributions [Fig. 10(b)] provide force boundary conditions that can be applied to a numerical soft tissue model for simulation purposes. The authors use the finite element method (FEM)-based linear elastostatic tissue model presented in Section III-A, and apply forces to mesh nodes that lie in the path of the needle. Fig. 16 shows a simulated needle insertion to a depth of 70 mm. Node displacements were found to closely match tracked marker motion measured in experiments. Maximum and mean node displacement errors of 1.4 and 0.6 mm are observed, respectively.

In a second simulation example, a needle is inserted into the side of a tissue model that is rigidly fixed along one edge, in order to investigate the effect of tissue deformation on needle placement accuracy. The needle axis is initially coincident with a “virtual biopsy target.” The series of simulation samples shown in Fig. 17 illustrates the needle’s path through the tissue sample, and its failure to intercept the target (shown as a black disk).

The simulation is physically based, but under specific conditions only. A user may command arbitrary needle velocities and may insert and retract the needle. A slip-stick force model was selected in order to permit such interaction, and the slip force threshold is set according to the shaft force distribution derived for insertions at a single velocity [37]. Therefore, simulated needle forces closely match measured values for insertions at this velocity. The force-velocity relationship measured in experiments is yet to be incorporated in the simulation algorithm.

VI. HAPTIC SIMULATION

A real-time implementation of the needle insertion simulator allows users to experience both visual and kinesthetic feedback while executing a virtual planar needle insertion, and is described in detail in [37].

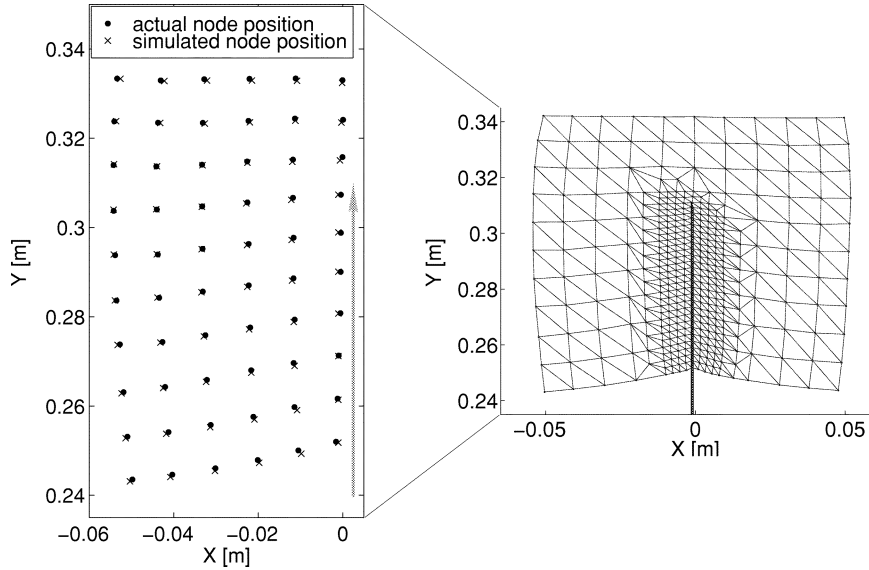


Fig. 16. Comparison between measured and simulated needle insertions (using the estimated force distribution). Left: a sample of the measured and simulated node positions from one half of the phantom (the deformation is symmetric).

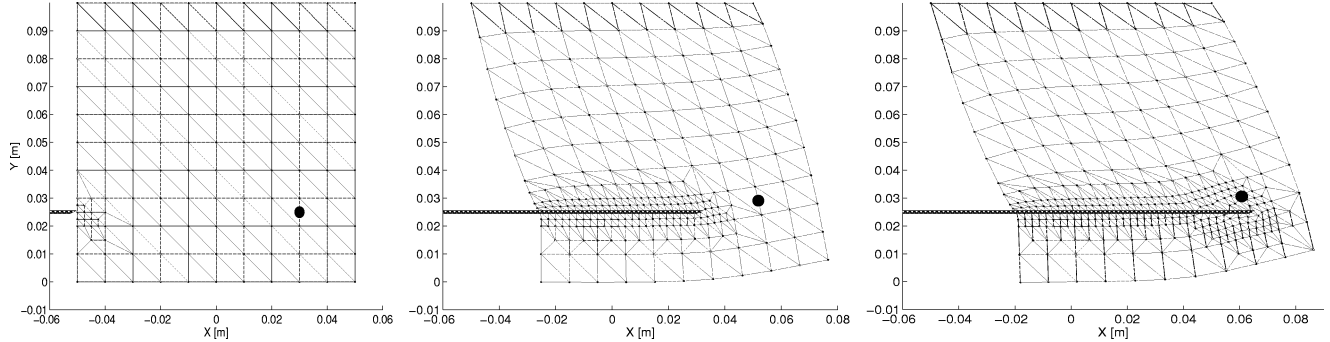


Fig. 17. Simulated needle intercept of a small target embedded within elastic tissue.

Real-time computation of the model described in Section V is complicated by the “curse of dimensionality” that is established by the large number of linear equations required to describe even small models. For example, a $10 \times 10 \times 10$ node 3-D volume results in 3000 linear equations in as many unknowns. It is clearly infeasible to solve such systems at haptic sample rates of 500 Hz and higher.

A. Condensing the Numerical System

The behavior of a continuum model discretised by the FEM is observed through the behavior of a finite set of mesh nodes. For large volumes of tissue that are finely discretised, the size of the matrix K in (4) becomes large due to the large number of material nodes at which force or displacement need to be computed. For needle insertion simulation, it is not necessary to consider the motion of nodes that are not visible (e.g., interior nodes), or the forces applied at nodes that are not in direct contact with the needle shaft. In Fig. 17, it is evident that the large majority of mesh nodes are neither visible nor palpable; therefore, the system of linear equations can be reduced to $\underline{u}_{\mathcal{W}} = K_{\mathcal{W}}^{-1} f_{\mathcal{W}}$, where only the behavior at a small subset \mathcal{W} of mesh nodes (called *working nodes*) is explicitly considered. At run time, the subset of working nodes \mathcal{W} is selected and the system matrix

reduced to $K_{\mathcal{W}}^{-1}$. As the needle penetrates the tissue surface, it intercepts hidden nodes that need to be reintroduced into the reduced system by simply adding new matrix rows and columns that are derived directly from K , which is precomputed. The matrix reduction approach is similar to the condensation techniques discussed in [38], and the boundary element method selected by [31]; however, in this paper, access to the interior of tissue volumes is retained for quick inclusion when needle penetration occurs.

B. Boundary Conditions and Needle Constraint

Mesh nodes that are in contact with the needle are constrained by the needle as shown in Fig. 18. If the needle is rigid, then the lateral position of the node is fixed along the 1x axis, which constitutes a *displacement boundary condition*. Along the needle shaft, the node force or node displacement may be constrained, depending upon its state of contact with the needle (e.g., sticking to the needle, or slipping) [37]. If the node is free to slide along the 1y axis, and a constant force consistent with the force distribution is applied to the slipping node. If it is in the *stuck* state, then the node is constrained to lie at a fixed point on the needle, along the 1y axis. Needle nodes switch from the *stuck*

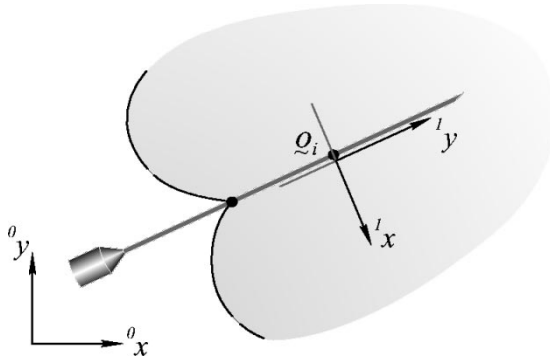


Fig. 18. Mesh nodes lying along the needle are constrained along the 1x axis, and either slip or stick along the 1y axis.

state to the *slip* state when their axial force exceeds that prescribed by the force distribution, as described in [37]. Therefore, when the virtual needle is being driven into the tissue model, the contact nodes slip along the needle and the estimated force distribution is applied along the shaft. The same force distribution is used regardless of axial needle velocity, even though it was experimentally determined for a single insertion rate of 1 mm/s.

The system of equations in $K_{\mathcal{W}}$ is rearranged in order to reflect the resulting inhomogeneous collection of boundary conditions

$$\underline{u}_{\mathcal{W}} = K_{\mathcal{W}}^{-1} \underline{f}_{\mathcal{W}} \rightarrow \underline{x}_{\mathcal{W}} = (K_{\mathcal{W}}^{-1})' \underline{y}_{\mathcal{W}} \quad (7)$$

where $\underline{x}_{\mathcal{W}}$ and $\underline{y}_{\mathcal{W}}$ are formed by exchanging elements between $\underline{u}_{\mathcal{W}}$ and $\underline{f}_{\mathcal{W}}$. Needle node boundary conditions change frequently during simulation, depending upon the commanded motion of the needle. A single boundary condition change of the i th coordinate can be expressed as an inexpensive low-rank update

$$(K_{\mathcal{W}}^{-1})' = K_{\mathcal{W}}^{-1} - \frac{\mathbf{c}_i \cdot \mathbf{r}_i}{p_i} \quad (8)$$

where p_i is the i th pivot of $K_{\mathcal{W}}^{-1}$; $[\mathbf{c}_i]_j = [K_{\mathcal{W}}^{-1}]_{ji}$ for $j \neq i$ and $[\mathbf{c}_i]_i = (p_i - 1)$; $[\mathbf{r}_i]_j = [K_{\mathcal{W}}^{-1}]_{ij}$ for $j \neq i$ and $[\mathbf{r}_i]_i = (p_i - 1)$. $(K_{\mathcal{W}}^{-1})'$ is the new system matrix and vectors $\underline{x}_{\mathcal{W}}$ and $\underline{y}_{\mathcal{W}}$ must be adjusted accordingly (i.e., by exchanging displacement and force variables). This approach to boundary condition changes results in an $O(N^2)$ computation rather than the $O(N^3)$ operation required to reinvert stiffness matrix $K_{\mathcal{W}}$, in a way that is similar to the capacitance matrix strategy presented by James and Pai in [31].

C. Local Coordinate Changes

The coordinate system shown in Fig. 18 is fixed to the needle; therefore, as its orientation changes, it is necessary to effect local coordinate changes in $K_{\mathcal{W}}^{-1}$. When the boundary conditions are uniform, this results in a simple affine transformation

$${}^0\underline{u}_{\mathcal{W}} = K_{\mathcal{W}}^{-10} \underline{f}_{\mathcal{W}} \Rightarrow {}^1\underline{u}_{\mathcal{W}} = A^T K_{\mathcal{W}}^{-1} A {}^1\underline{f}_{\mathcal{W}} \quad (9)$$

where ${}^0\underline{u}_{\mathcal{W}}$ and ${}^0\underline{f}_{\mathcal{W}}$ are displacement and force vectors in a nominal system coordinate frame, while ${}^1\underline{u}_{\mathcal{W}}$ and ${}^1\underline{f}_{\mathcal{W}}$ are the vectors after rotating the coordinate frame at the i th node by an angle θ . Matrix A is composed of (2×2) rotation submatrices

on its diagonal. Details of this transformation are given in the Appendix and in [37].

If node i has different boundary conditions along its two coordinate axes, then such a transformation is not possible, due to the mixed force and displacement variables in $\underline{x}_{\mathcal{W}}$ and $\underline{y}_{\mathcal{W}}$. The local coordinate transformation for a node that is sliding along the needle axis has the following form:

$${}^1\underline{x}_{\mathcal{W}} = (M - K_{\mathcal{W}}^{-1} N)^{-1} (K_{\mathcal{W}}^{-1} M - N) {}^1\underline{y}_{\mathcal{W}} \quad (10)$$

where M and N are sparse transformation matrices. Due to the properties of M and N , $(M - K_{\mathcal{W}}^{-1} N)$ is shown in the Appendix to be inexpensively inverted [37]. Node coordinate frames must be updated incrementally from one simulation sample period to the next, according to the change in needle orientation angle $\Delta\theta$. If the needle is curved or flexible, then the local coordinate system transformations will vary along the length of the needle shaft.

D. System Solution

The reduced system matrix $K_{\mathcal{W}}^{-1}$ evolves from sample period to sample period, due to boundary condition and local coordinate system updates, and is used to solve for $\underline{x}_{\mathcal{W}}$, the vector of unknown node forces and displacements. Node positions are updated for graphical rendering of the scene, and needle node forces are integrated for feedback via the haptic interface. The interactive real-time model shown in Fig. 19 consists of 361 nodes and is computed at a rate of 500 Hz, without any particular effort to optimize code.

E. Discussion

The linear elastostatic model discretised by finite element analysis has worked well for the PVC phantoms. Local phantom stresses due to the observed needle force distribution are fairly low, so that axial strains are low. There is little lateral motion and rotation during typical needle trajectories; however, users are not constrained during haptic simulation and may generate large strains. More complex material models may be substituted in order to account for these large strains and perhaps nonlinear constitutive behavior, without affecting the force distribution modeling methodology presented here. However, not all models will be amenable to real-time simulation.

VII. CONCLUSION

Needle mechanics measurements and simulations are of interest for the development of physically based virtual planning and training systems that are aimed at reducing the incidence of complications in clinical practice. This paper presents a novel approach for estimating needle shaft forces and tissue behavior using a tissue measurement system and soft tissue deformation models. Force estimates were used in simulation to compute tissue model deformation, as well as to predict target motion and needle trajectories due to tissue deformation. The integral of the estimated shaft force distribution was found to be in close agreement with driving forces measured at the base of the needle during experiments. In addition, simulated phantom deformations match measured phantom deformations, indicating that the method works well.

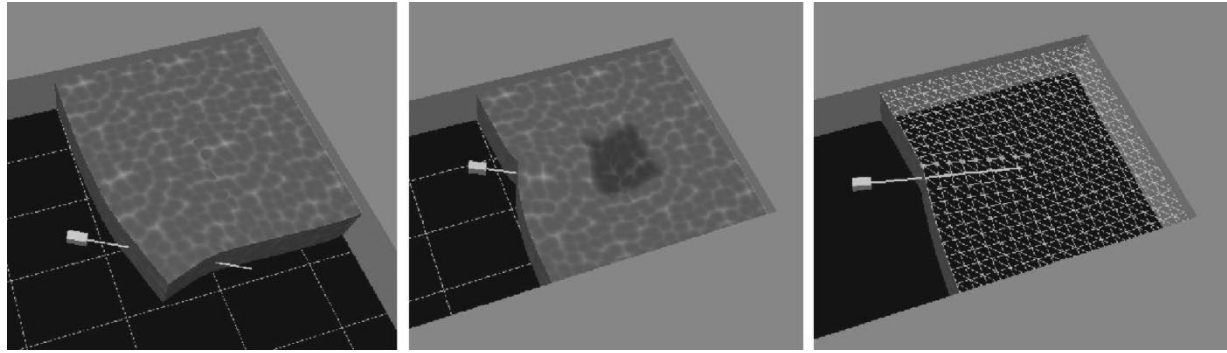


Fig. 19. Interactive virtual needle insertion in a planar environment.

We have developed a fast, optimized simulation algorithm for interactive needle insertion by judicious application of a condensation technique that reduces computation and permits the simulation of significant models at high sample rates on an ordinary PC. Unlike existing single-axis simulation, steering torques and lateral needle forces can be felt, while tissue deformation is observed, illustrating the potential of physically based needle insertion simulations for planning and training purposes. The approach is generalizable to three dimensions (3-D simulation has recently been explored in [39]).

Future work will explore tissue measurement and characterization, model-based planning, and the control of needle insertion procedures using models developed in this paper.

APPENDIX

For local coordinate changes at free traction nodes, or fully displacement-constrained nodes, the matrix A in (9) is (2×2) block diagonal

$$A = \begin{bmatrix} 1 & 0 & \dots & 0 & 0 & \dots & 0 \\ 0 & 1 & & 0 & 0 & & 0 \\ \vdots & \ddots & & & & & \vdots \\ 0 & 0 & & \cos(\theta) & -\sin(\theta) & & 0 \\ 0 & 0 & & \sin(\theta) & \cos(\theta) & & 0 \\ \vdots & & & & & \ddots & \vdots \\ 0 & 0 & \dots & 0 & 0 & \dots & 1 \end{bmatrix}.$$

In (10), the local coordinate transformation for a node that is in the *slip* state is computed, where M and N are defined as follows:

$$M = \begin{bmatrix} 1 & 0 & \dots & 0 & 0 & \dots & 0 \\ 0 & 1 & & 0 & 0 & & 0 \\ \vdots & \ddots & & & & & \vdots \\ 0 & 0 & & \cos(\theta) & 0 & & 0 \\ 0 & 0 & & 0 & \cos(\theta) & & 0 \\ \vdots & & & & & \ddots & \vdots \\ 0 & 0 & \dots & 0 & 0 & \dots & 1 \end{bmatrix}$$

$$N = \begin{bmatrix} 0 & 0 & \dots & 0 & 0 & \dots & 0 \\ 0 & 0 & & 0 & 0 & & 0 \\ \vdots & & \ddots & & & & \vdots \\ 0 & 0 & & 0 & -\sin(\theta) & & 0 \\ 0 & 0 & & \sin(\theta) & 0 & & 0 \\ \vdots & & & & & \ddots & \vdots \\ 0 & 0 & \dots & 0 & 0 & \dots & 0 \end{bmatrix}.$$

The matrix transformation $(K_{\mathcal{W}}^{-1} M - N)$ amounts to changes in only two columns of the $K_{\mathcal{W}}^{-1}$ matrix; however, $(M - K_{\mathcal{W}}^{-1} N)$ must still be inverted. This matrix inverse is shown to be sparsely populated, with analytical inverse given by

$$(M - K_{\mathcal{W}}^{-1} N)^{-1} = \begin{bmatrix} 1 & 0 & \dots & a_{(1,2i)} & a_{(1,2i+1)} & \dots & 0 \\ 0 & 1 & & a_{(2,2i)} & a_{(2,2i+1)} & & 0 \\ \vdots & \ddots & & & & & \vdots \\ 0 & 0 & & a_{(2i,2i)} & a_{(2i,2i+1)} & & 0 \\ 0 & 0 & & a_{(2i+1,2i)} & a_{(2i+1,2i+1)} & & 0 \\ \vdots & & & & & \ddots & \vdots \\ 0 & 0 & \dots & a_{(2s,2i)} & a_{(2s,2i+1)} & \dots & 1 \end{bmatrix}.$$

where

$$a_{(1,2i)} = -\frac{\sin \theta [k_{(1,2i+1)} (\cos \theta + k_{(2i+1,2i)} \sin \theta)]}{\sum} + \frac{\sin \theta [k_{(1,2i)} k_{(2i+1,2i+1)} \sin \theta]}{\sum}$$

$$a_{(1,2i+1)} = \frac{\sin \theta [k_{(1,2i)} (\cos \theta - k_{(2i,2i+1)} \sin \theta)]}{\sum} + \frac{\sin \theta [k_{(1,2i+1)} k_{(2i,2i)} \sin \theta]}{\sum}$$

$$a_{(2i,2i)} = -\frac{\cos \theta + k_{(2i+1,2i)} \sin \theta}{\sum}$$

$$a_{(2i,2i+1)} = \frac{k_{(2i,2i)} \sin \theta}{\sum}$$

$$a_{(2i+1,2i)} = -\frac{k_{(2i+1,2i+1)} \sin \theta}{\sum}$$

$$a_{(2i+1,2i+1)} = \frac{-\cos \theta + k_{(2i,2i+1)} \sin \theta}{\sum}$$

$$\sum = -\cos^2 \theta + \cos \theta \sin \theta$$

$$\times (k_{(2i,2i+1)} - k_{(2i+1,2i)})$$

$$+ \sin^2 \theta (k_{(2i,2i+1)} k_{(2i+1,2i)})$$

$$- k_{(2i,2i)} k_{(2i+1,2i+1)})$$

and $k_{(m,n)}$ is the element at the m th row and n th column of $K_{\mathcal{W}}^{-1}$

REFERENCES

- [1] F. S. Azar, D. N. Metaxas, and M. D. Schnall, "A finite element model of the breast for predicting mechanical deformations during biopsy procedures," in *Proc. IEEE Workshop Mathematical Methods in Biomedical Image Analysis*, 2000, pp. 38–45.
- [2] S. Nath, Z. Chen, N. Yue, S. Trumppore, and R. Peschel, "Dosimetric effects of needle divergence in prostate seed implant using ^{125}I and ^{103}Pd radioactive seeds," *Med. Phys.*, pp. 1058–1066, 2000.
- [3] J. De Andres, M. A. Reina, and A. Lopez-Garcia, Risks of regional anaesthesia: Role of equipment—Needle design, catheters. presented at Proc. 17th Annu. Eur. Soc. Regional Anaesthesia Congr. [Online] Available: <http://www.esraeurope.org/andres14.htm>.
- [4] S. Datta, Complications of regional analgesia and anaesthesia. presented at Proc. 17th Annu. Eur. Soc. Regional Anaesthesia Congr. [Online] Available: <http://www.esraeurope.org/datta1.htm>.
- [5] B. Finucane, Complications of brachial plexus anaesthesia. presented at Proc. 17th Annu. Eur. Soc. Regional Anaesthesia Congr. [Online] Available: <http://www.esraeurope.org.finucan1.htm>.
- [6] D. L. Brown, What do we need to advance regional anaesthesia?. presented at Proc. Annu. Eur. Soc. Regional Anaesthesia Congr. [Online] Available: <http://www.esraeurope.org.brown12.htm>.
- [7] E. Gobbetti, M. Tuveri, G. Zanetti, and A. Zorcolo, "Catheter insertion simulation with co-registered direct volume rendering and haptic feedback," in *Proc. Medicine Meets Virtual Reality 2000*, Jan. 2000, pp. 96–98.
- [8] CathSim Vascular Access Simulator. Immersion Medical. [Online]. Available: <http://www.immersion.com/products/medical/vascular.shtml>
- [9] P. N. Brett, T. J. Parker, A. J. Harrison, T. A. Thomas, and A. Carr, "Simulation of resistance forces acting on surgical needles," *Inst. Mech. Eng. Part H, J. Eng. Med.*, vol. 211, pp. 335–347, 1997.
- [10] P. Gorman, T. Krummel, R. Webster, M. Smith, and D. Hutchens, "A prototype haptic lumbar puncture simulator," in *Proc. Medicine Meets Virtual Reality*, 2000, pp. 106–109.
- [11] T. Dang, T. M. Annaswamy, and M. A. Srinivasan, "Development and evaluation of an epidural injection simulator with force feedback for medical training," in *Proc. Medicine Meets Virtual Reality*, 2001, pp. 97–102.
- [12] D.-S. Kwon, J.-U. Kyung, S. M. Kwon, J. B. Ra, H. W. Park, H. S. Kang, J. Zeng, and K. R. Cleary, "Realistic force reflection in a spine biopsy simulator," in *IEEE Int. Conf. Robotics and Automation*, 2001, pp. 1358–1363.
- [13] K. B. Shimoga and P. K. Khosla, "Visual and force feedback to aid neurosurgical probe insertion," in *Proc. 16th Int. Conf. IEEE Engineering in Medicine and Biology Society*, vol. 2, 1994, pp. 1051–1052.
- [14] S. Miller, C. Jeffrey, J. Bews, and W. Kinsner, "Advances in the virtual reality interstitial brachytherapy system," in *Proc. Canadian Conf. Electronics and Computer Engineering*, May 1999, pp. 349–354.
- [15] J. Zeng, C. Kaplan, J. Bauer, J. Xuan, I. A. Sesterhenn, J. H. Lynch, M. T. Freedman, and S. K. Mun, "Optimizing prostate needle biopsy through 3-D simulation," *Proc. SPIE Medical Imaging*, vol. 3335, pp. 488–497, Feb. 1998.
- [16] D. Sorid and S. K. Moore, "The virtual surgeon," *IEEE Spectr.*, pp. 26–31, July 2000.
- [17] L. M. Auer, A. Radetzky, C. Wimmer, G. Kleinszig, F. Schroecker, D. P. Auer, H. Delingette, B. Davies, and D. P. Pretschner, "Visualization for planning and simulation of minimally invasive neurosurgical procedures," in *Proc. Medical Image Computing and Computer-Assisted Intervention*, 1999, pp. 1199–1209.
- [18] A. Zivanovic and B. L. Davies, "A robotic system for blood sampling," *IEEE Trans. Inform. Technol. Biomed.*, vol. 4, pp. 8–14, Mar. 2000.
- [19] K. Khodabandehloo, P. N. Brett, and R. O. Buckingham, "Special-purpose actuators and architectures for surgery robots," in *Computer-Integrated Surgery: Technology and Clinical Applications*. Cambridge, MA: MIT Press, 1996.
- [20] L. Hiemenz, D. J. McDonald, D. Stredney, and D. Sessanna, "A physiologically valid simulator for training residents to perform an epidural block," in *Proc. 15th Southern Biomedical Engineering Conf.*, Mar. 1996, pp. 170–173.
- [21] L. Hiemenz, A. Litsky, and P. Schmalbrock, Puncture mechanics for the insertion of an epidural needle. presented at Proc. 21st Annu. Meeting American Society of Biomechanics. [Online] Available: <http://asb-biomech.org/onlineabs/abstracts97/34/index.html>.
- [22] C. Simone and A. M. Okamura, "Modeling of needle insertion forces for robot-assisted percutaneous therapy," in *Proc. Int. Conf. Robotics and Automation*, May 2002, pp. 2085–2091.
- [23] R. Alterovitz, J. Pouliot, R. Taschereau, I.-C. J. Hsu, and K. Goldberg, "Needle insertion and radioactive seed implantation in human tissues: Simulation and sensitivity analysis," in *IEEE Int. Conf. Robotics and Automation*, 2003, to be published.
- [24] M. R. Sirosipour, S. P. DiMaio, S. E. Salcudean, P. Abolmaesumi, and C. Jones, "Haptic interface control—Design issues and experiments with a planar device," in *Proc. IEEE Int. Conf. Robotics and Automation*, Apr. 2000, pp. 24–28.
- [25] Y. C. Fung, *Biomechanics—Mechanical Properties of Living Tissues*. New York: Springer-Verlag, 1993.
- [26] K. Miller, K. Chinzei, G. Orsengo, and P. Bednarz, "Mechanical properties of brain tissue *in-vivo*: Experiment and computer simulation," *J. Biomech.*, vol. 33, pp. 1369–1376, 2000.
- [27] M. P. Ottensmeyer and J. K. Salisbury, Jr., "In vivo data acquisition instrument for solid organ mechanical property measurement," *Proc. Medical Image Computing and Computer Aided Intervention (MICCAI)*, pp. 975–982, 2001.
- [28] I. Brouwer *et al.*, "Measuring *in vivo* animal soft tissue properties for haptic modeling in surgical simulation," in *Medicine Meets Virtual Reality*, J. D. Westwood *et al.*, Eds. Amsterdam, The Netherlands: IOS Press, 2001, pp. 69–74.
- [29] J. Heikkilä and O. Silvén, "A four-step camera calibration procedure with implicit image correction," in *Proc. IEEE Comput. Soc. Conf. Computer Vision and Pattern Recognition (CVPR'97)*, 1997, pp. 1106–1112.
- [30] A. E. Kerdok, S. M. Cotin, M. P. Ottensmeyer, A. Galea, R. D. Howe, and S. L. Dawson, "Truth cube: Establishing physical standards for real-time soft tissue simulation," in *Proc. Int. Workshop on Deformable Modeling and Soft Tissue Simulation*, Nov. 2001, pp. 65–72.
- [31] D. L. James and D. K. Pai, "ArtDefo, accurate real-time deformable objects," in *Proc. SIGGRAPH'99, Computer Graphics*, 1999.
- [32] S. Cotin, H. Delingette, and N. Ayache, "Real-time elastic deformations of soft tissues for surgery simulation," *IEEE Trans. Visual. Comput. Graphics*, vol. 5, pp. 62–73, Jan. 1999.
- [33] A. Hagemann, K. Rohr, H. S. Stiehl, U. Spetzger, and J. M. Gilsbach, "Nonrigid matching of tomographic images based on a biomechanical model of the human head," *Med. Imaging—Image Processing*, pp. 583–592, 1999.
- [34] Y. C. Fung, *A First Course in Continuum Mechanics*. Englewood Cliffs, NJ: Prentice-Hall, 1977.
- [35] C. Cuvelier, A. Segal, and A. A. van Steenhoven, *Finite Element Methods and Navier-Stokes Equations*. Amsterdam, The Netherlands: Reidel, 1986.
- [36] H. Kataoka, T. Washio, K. Chinzei, K. Mizuhara, C. Simone, and A. M. Okamura, "Measurement of the tip and friction force acting on a needle during penetration," in *Proc. Medical Image Computing and Computer Aided Intervention*, 2002, pp. 216–223.
- [37] S. P. DiMaio and S. E. Salcudean, "Simulated interactive needle insertion," in *Proc. 10th Symp. Haptic Interfaces for Virtual Environment, Teleoperator Systems*, Mar. 24–25 2002, pp. 344–351.
- [38] M. Bro-Nielsen, "Finite element modeling in surgery simulation," *Proc. IEEE*, vol. 86, pp. 490–503, 1998.
- [39] H.-W. Nienhuys and A. F. van der Stappen. (2003) Interactive Needle Insertions in 3-D Nonlinear Material. Inst. Inform. Comput. Sci., Utrecht Univ., Utrecht, The Netherlands. [Online]. Available: www.cs.uu.nl



Simon P. DiMaio (S'98) received the B.Sc. degree in electrical engineering from the University of Cape Town, Cape Town, South Africa, in 1995. In 1998, he completed the M.A.Sc. degree at the University of British Columbia, Vancouver, BC, Canada, where he is currently working toward the Ph.D. degree in electrical engineering.

His research interests include the control of robotic mechanisms, environment model identification, virtual environment simulation, medical simulation, and haptics.



S. E. Salcudean (S'78–M'79–SM'03) received the B. Eng. and M.Eng. degrees from McGill University, Montreal, QC, Canada, and the Ph.D. degree from the University of California at Berkeley, all in electrical engineering.

From 1986 to 1989, he was a Research Staff Member in the robotics group at the IBM T.J. Watson Research Center. He then joined the Department of Electrical and Computer Engineering at the University of British Columbia, Vancouver, BC, Canada, where he is now a Professor and holds a

Canada Research Chair. He spent one year at ONERA in Toulouse, France, in 1996–1997, where he held a Killam Research Fellowship. He is interested in haptic interfaces, teleoperation, and virtual environments. He is pursuing applications to medical diagnosis and interventions and to the control of heavy-duty hydraulic machines such as excavators.

Dr. Salcudean has been a co-organizer of several symposia on haptic interfaces and a technical and senior Editor of the IEEE TRANSACTIONS ON ROBOTICS AND AUTOMATION.